

Structural, Magnetic, Magnetocaloric, and Magnetostrictive Properties of $\text{Pb}_{1-x}\text{Sr}_x\text{MnBO}_4$ ($x = 0, 0.5, \text{ and } 1.0$)

Jake Head, Pascal Manuel, Fabio Orlandi, Minki Jeong, Martin R. Lees, Rukang Li, and Colin Greaves*



Cite This: *Chem. Mater.* 2020, 32, 10184–10199



Read Online

ACCESS |



Metrics & More

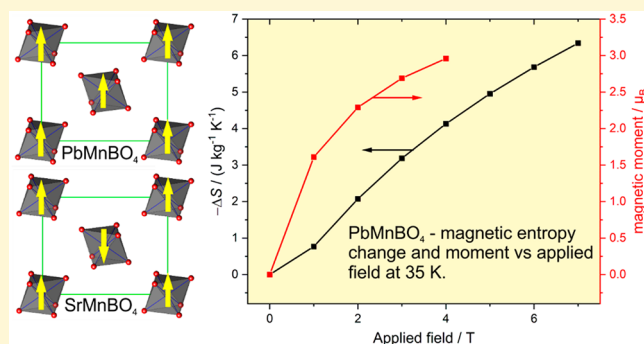


Article Recommendations



Supporting Information

ABSTRACT: The solid solution $\text{Pb}_{1-x}\text{Sr}_x\text{MnBO}_4$ is reported with an orthorhombic, $Pnma$, structure throughout; here studies on compounds with $x = 0, 0.5, \text{ and } 1$ are described. The structure contains chains of MnO_6 octahedra that exhibit intra-chain ferromagnetic (FM) order at low temperatures. Neutron powder diffraction (NPD) reveals a dominant FM order in PbMnBO_4 ($T_c = 30$ K), whereas SrMnBO_4 is primarily antiferromagnetic (AFM) with $T_N = 16$ K; the difference is related to the link between the chains that involves the BO_3 groups. PbMnBO_4 has its moment along a but also has a previously unreported AFM contribution along c (magnetic space group $Pnm'a'$), whereas SrMnBO_4 has its moment along a but also a FM canting along c (magnetic space group $Pn'm'a$). The end members show distinct magnetostriction at T_c/T_N which correlates with the different magnetic exchange in these compounds. NPD in variable applied magnetic field shows that SrMnBO_4 is converted to fully FM at 8 T. The behavior above the magnetic ordering temperature is consistent with short-range FM correlations within the chains, which is particularly apparent in PbMnBO_4 . The magnetocaloric effect (MCE) has been measured and compared with those previously reported for the mineral gaudfroyite. PbMnBO_4 has excellent MCE behavior, especially near T_c , 30 K. The strong FM exchange within the chains and FM correlations above T_c are vital for the MC properties.



INTRODUCTION

The magnetocaloric effect (MCE) is an important phenomenon which can result in a large temperature decrease if a magnetic field applied to a magnetic material is reduced to zero under adiabatic conditions. The effect relates directly to the positive entropy change (ΔS) that occurs when the magnetic field is removed and the moments disorder; typically, it is largest near the Curie temperature for a paramagnet-ferromagnet phase transition but is also large for paramagnetic lanthanide compounds at low temperatures. The adiabatic conditions determine that ΔS causes cooling of the material. Adiabatic magnetic cooling is highly attractive because it potentially has an energy efficiency approaching 100% of the Carnot maximum and has recently attracted much attention for ambient temperature refrigeration.^{1–3} However there remains a significant need for MCE materials for low temperature applications, especially near 20 K for efficient liquefaction of hydrogen.^{4–7} This will become more important as hydrogen features strongly in an energy framework, and the production of liquid hydrogen will be critical for storage and transport. The most practical material is $\text{Gd}_3(\text{Ga,Fe})_5\text{O}_{12}$ (GGIG), but its MCE is still small with $\Delta S = -7.5 \text{ J kg}^{-1} \text{ K}^{-1}$ at 20 K with a field change of 5 T.⁷ Although intermetallics, e.g., RAl_2 ($R = \text{rare earth}$) can have very good MCE properties at ~ 20 K,⁸ they lack the necessary chemical stability in the presence of gaseous and liquid H_2 .⁷ There

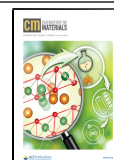
remains, therefore, a need for materials which display the required characteristics for hydrogen liquefaction: high entropy change at ~ 20 K using relatively low field changes (~ 2 T) which can be achieved without using superconducting magnets; a rapid response to the change in field. Ideally, the materials would be lanthanide-free to avoid possible issues with sustainability.

Frustrated magnetic materials were predicted to offer high potential for improved MCE properties (especially low field behavior and speed of temperature response) in accordance with theoretical considerations.^{9,10} The predicted advances were based on the highly degenerate magnetic ground states in Kagomé, garnet, and pyrochlore lattices or even molecular systems. These predictions were subsequently confirmed experimentally for the pyrochlore $\text{Gd}_2\text{Ti}_2\text{O}_7$.¹¹ Some magnetically frustrated metal organic framework materials containing chains of lanthanide ions, e.g., $\text{Ln}(\text{HCOO})_3$ ($\text{Ln} = \text{lanthanide}$) have also shown excellent MCE properties, but their efficacy is

Received: September 17, 2020

Revised: November 7, 2020

Published: November 17, 2020



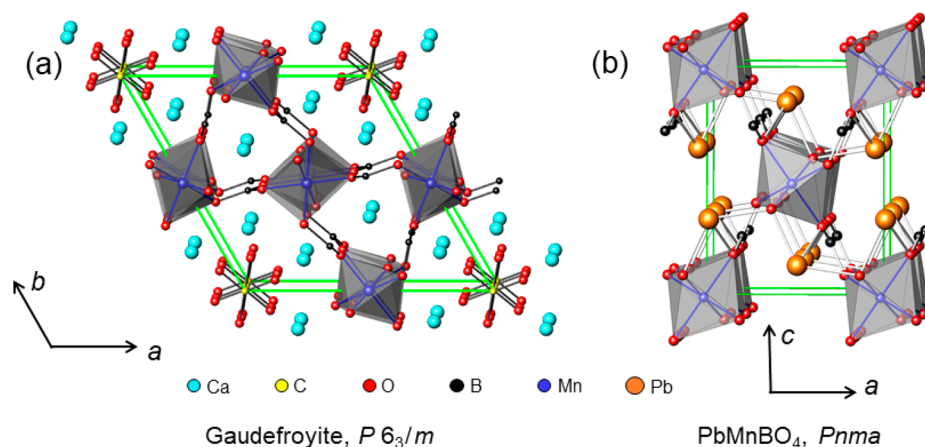


Figure 1. Structures of (a) gaufreyite and (b) $PbMnBO_4$ viewed along the chains of MnO_6 octahedra.

highest below 4 K.^{12–15} The mineral gaufreyite [$Ca_4Mn_3O_3(BO_3)_3(CO_3)$] is hexagonal, $P6_3/m$, with 1D chains of edge-linked $Mn^{3+}O_6$ octahedra¹⁶ and the Mn ions located on a 2D Kagomé lattice perpendicular to the chains (Figure 1a); it was demonstrated to have excellent low-field MCE properties: from 0–2 T, $\Delta S = -7 \text{ J kg}^{-1} \text{ K}^{-1}$ at 11 K and $\Delta S = -4 \text{ J kg}^{-1} \text{ K}^{-1}$ at 20 K.¹⁷ The structural and magnetic features considered to be important for these properties are as follows:

- each Mn chain displays ferromagnetic (FM) coupling
- antiferromagnetic (AFM) exchange between the chains is frustrated and results in a $q = 0$ structure with 120° between the magnetic moments below 10.2 K ¹⁸
- short-range FM order within the chains above T_N allows for good low-field MCE behavior for $T > T_N$

Figure 1a shows that the chains of octahedra are linked by planar borate (BO_3^{3-}) groups to form channels between the chains; these are occupied by Ca^{2+} ions and disordered carbonate (CO_3^{2-}) ions. The MCE properties of gaufreyite encouraged us to look for materials with related structural and magnetic characteristics. $PbMnBO_4$ was of particular interest and has an orthorhombic structure, $Pnma$, with similar chains of MnO_6 octahedra parallel to the b -axis (Figure 1b), which now display both intra- and inter-chain FM order below $\sim 31 \text{ K}$.¹⁹ Although not magnetically frustrated, density functional theory calculations indicate that the intra-chain exchange constant is 1 order of magnitude larger than that for inter-chain exchange.^{20,21} In addition, there is strong experimental evidence for short-range FM order within the chains at temperatures significantly above T_c from magnetic measurements,¹⁹ specific heat measurements,²² and ferromagnetic resonance.²³

Notwithstanding the weight penalty of containing Pb, the interesting magnetic properties of $PbMnBO_4$, and the absence of magnetic frustration in contrast to gaufreyite, a detailed neutron powder diffraction (NPD) study of its structural and magnetic behavior in magnetic fields has been conducted in order to provide guidance for new materials for practical MCE behavior near 20 K. The study also resulted in the synthesis of two new compounds, $SrMnBO_4$ and $Pb_{0.5}Sr_{0.5}MnBO_4$, which, although structurally related to $PbMnBO_4$, display very different magnetic behavior. These differences provide a basis for the discussion of the magnetic exchange interactions in these phases and useful experimental data for designing new

MCE materials. The MCE properties of all materials were measured.

EXPERIMENTAL METHODS

The samples examined were synthesized from Sigma-Aldrich chemicals: Mn_2O_3 (99.9%), PbO (99.9%), $SrCO_3$ (99.9%), and $^{11}B_2O_3$ (>99% ^{11}B). The ^{11}B -enriched B_2O_3 was initially converted to H_3BO_3 by dissolving it in the minimum amount of H_2O and drying overnight at 60°C . At higher temperatures partial dehydration to HBO_2 can occur. For the synthesis of $PbMnBO_4$, the problems reported previously¹⁹ were not encountered and phase pure samples were obtained from well-mixed PbO , Mn_2O_3 , and H_3BO_3 by slow heating (40°C h^{-1}) to 700°C and holding for 10 h. This process was repeated for all samples used for characterization. $SrMnBO_4$ was more difficult to obtain phase pure than the Pb-containing samples, presumably because of PbO acting as a flux in the latter materials. $SrMnBO_4$ was synthesized by heating a mixture of $SrCO_3$, Mn_2O_3 , and H_3BO_3 at 25°C h^{-1} to 850°C and holding for 3 h followed by 10°C h^{-1} to 950°C and holding for 30 h. This process was repeated to obtain the highest level of purity. $Pb_{0.5}Sr_{0.5}MnBO_4$ was synthesized from two heat treatments, each comprising 50°C h^{-1} to 850°C and holding for 6 h.

The initial structure and sample purity characterization was achieved by X-ray powder diffraction (XRPD; Bruker D8 Advance, $Cu K\alpha$ radiation in reflection mode). NPD data were collected on the instrument WISH at ISIS, Science and Technology Facilities Council, Rutherford Appleton Laboratory.²⁴ This diffractometer provides high-quality data at low- Q and is therefore ideal for magnetic measurements. Four pairs of detectors were used, located at approximate 2θ values of 153° (highest resolution, high Q), 122° , 90° , and 58° (lower resolution, low Q); equal weighting was applied to all detectors used in the refinements. Data were collected at ambient temperature and temperatures down to 1.5 K (cryostat for $Pb_{0.5}Sr_{0.5}MnBO_4$, cryomagnet for $PbMnBO_4$ and $SrMnBO_4$); the cryomagnet produced data for $SrMnBO_4$ and $PbMnBO_4$ in applied fields up to 8 T. $Pb_{0.5}Sr_{0.5}MnBO_4$ was in powdered form ($\sim 2 \text{ g}$ in a 6 mm diameter V can), whereas $PbMnBO_4$ (4.8 g) and $SrMnBO_4$ (4.2 g) were converted into discs (7 mm diameter, $\sim 5 \text{ mm}$ thick) which were sintered at the final synthesis temperature, to prevent sample movement in high fields, and loaded into 8 mm cans. Calculations of μ_r/r indicated that absorption corrections were unnecessary because of the use of ^{11}B . Structure refinements based on the NPD datasets were achieved using the GSAS-II software package.²⁵

Magnetic susceptibility measurements were obtained from a Quantum Design MPMS magnetometer. Zero field-cooled (ZFC) and field-cooled (FC) data were obtained on warming after cooling the samples in zero field and the measuring field (10 mT), respectively. The magnetic entropy change ΔS at a given field and temperature was determined indirectly²⁶ from one of the Maxwell

Table 1. Structural Parameters for PbMnBO₄ at 300 K (Top Line) and 1.5 K (Bottom Line)^a

atom	site	T/K	x/a	y/b	z/c	100×U _{iso} /Å ²
Pb	4c	300	0.0335(5)	0.25	0.3526(3)	1.14(6)
		1.5	0.0382(2)			0.51(6)
Mn	4a	300	0	0	0	2.0(2)
		1.5				0.9(1)
O1	4c	300	0.1088(7)	0.75	0.8952(5)	1.1(1)
		1.5	0.1081(3)			1.4(1)
O2	8d	300	0.1687(5)	0.9544(3)	0.1881(3)	1.16(7)
		1.5	0.1666(3)	0.9532(3)	0.1891(2)	0.71(6)
O3	4c	300	0.7884(7)	0.75	0.0928(4)	1.5(1)
		1.5	0.7874(3)			0.70(8)
B	4c	300	0.7927(6)	0.25	0.7380(4)	1.32(9)
		1.5	0.7919(3)			0.57(8)

^aSpace group *Pnma*; 300 K: *a* = 6.69380(5) Å; *b* = 5.94182(4) Å; *c* = 8.63691(7) Å. 1.5 K: *a* = 6.7078(1) Å; *b* = 5.93651(7) Å; *c* = 8.6063(1) Å. Magnetic moment (*Pnm'a'*) at 1.5 K: $\mu_x = 3.42(4) \mu_B$; $\mu_y = 0 \mu_B$; $\mu_z = 0.41(6) \mu_B$; $\mu_{total} = 3.44(4) \mu_B$. Overall wR_p : 0.052 (153° + 122° detectors, 300 K); 0.078 (122° + 90° detectors, 1.5 K).

Table 2. Structural Parameters for Pb_{0.5}Sr_{0.5}MnBO₄ at 300 K (Top Line) and 1.5 K (Bottom Line)^a

atom	site	T/K	x/a	y/b	z/c	100×U _{iso} /Å ²
Pb/Sr ^b	4c	300	0.0017(3)	0.25	0.3532(4)	2.2(1)
		1.5	-0.0007(3)			0.80(7)
Mn	4a	300	0	0	0	0.4(2)
		1.5				0.9(1)
O1	4c	300	0.111(1)	0.75	0.8996(5)	1.1(1)
		1.5	0.1190(3)			1.02(9)
O2	8d	300	0.1652(8)	0.9551(4)	0.1822(2)	2.3(1)
		1.5	0.1771(3)	0.9526(2)	0.1826(2)	1.11(6)
O3	4c	300	0.749(1)	0.75	0.0964(5)	3.7(2)
		1.5	0.7583(3)			1.03(9)
B	4c	300	0.8026(7)	0.25	0.7440(4)	0.6(1)
		1.5	0.7987(3)			0.75(7)

^aSpace group *Pnma*; 300 K: *a* = 6.31306(9) Å; *b* = 5.97078(6) Å; *c* = 8.87951(9) Å. 1.5 K: *a* = 6.2989(1) Å; *b* = 5.96542(7) Å; *c* = 8.8742(1) Å. Magnetic moment (*Pn'm'a'*) at 1.5 K: $\mu_x = 3.71(1) \mu_B$; $\mu_y = 0 \mu_B$; $\mu_z = 0.0 \mu_B$; $\mu_{total} = 3.71(1) \mu_B$. Overall wR_p : 0.063 (153° + 122° detectors, 300 K); 0.064 (122° + 58° detectors, 1.5 K). ^bThe Pb/Sr site occupancy was constrained to 0.5/0.5 since refinement resulted in no change.

Table 3. Structural Parameters for SrMnBO₄ at 300 K (Top Line) and 1.5 K (Bottom Line)^a

atom	site	T/K	x/a	y/b	z/c	100×U _{iso} /Å ²
Sr	4c	300	-0.0119(3)	0.25	0.3555(2)	0.57(6)
		1.5	-0.0136(3)			0.50(8)
Mn	4a	300	0	0	0	0.9(1)
		1.5				0.8(1)
O1	4c	300	0.1164(5)	0.75	0.9092(3)	0.72(8)
		1.5	0.1254(3)			1.40(9)
O2	8d	300	0.1727(4)	0.9540(3)	0.1802(2)	0.99(5)
		1.5	0.1754(3)	0.9511(2)	0.1826(2)	1.28(6)
O3	4c	300	0.7320(5)	0.75	0.0940(3)	0.92(7)
		1.5	0.7334(3)			0.97(8)
B	4c	300	0.8104(4)	0.25	0.7435(3)	1.05(6)
		1.5	0.8065(3)			0.33(6)

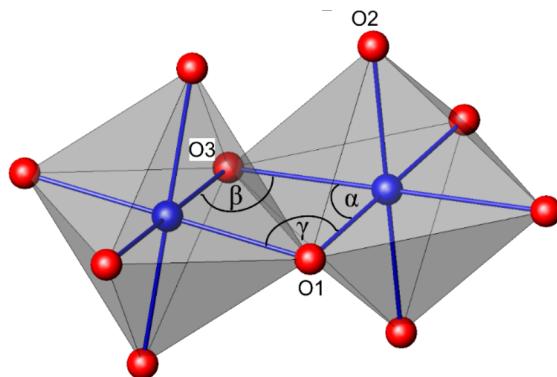
^aSpace group *Pnma*; 300 K: *a* = 6.14892(3) Å; *b* = 5.97768(4) Å; *c* = 8.97067(6) Å. 1.5 K: *a* = 6.12975(5) Å; *b* = 5.97004(6) Å; *c* = 8.9545(1) Å. Magnetic moment (*Pn'm'a'*) at 1.5 K: $\mu_x = 3.42(4) \mu_B$; $\mu_y = 0 \mu_B$; $\mu_z = 0.0 \mu_B$; $\mu_{total} = 3.42(4) \mu_B$. Overall wR_p : 0.040 (153° + 122° detectors, 300 K); 0.059 (122° + 58° detectors, 1.5 K).

thermodynamic relations using magnetization versus magnetic field data collected in an Oxford Instruments vibrating sample magnetometer.

RESULTS AND DISCUSSION

Nuclear Structures at Ambient Temperature and 1.5 K. The chains of MnO₆ octahedra in PbMnBO₄ are linked by B

atoms (within BO₃ groups) and also Pb²⁺ ions (Figure 1b). The Pb²⁺ ions are bonded to four O²⁻ ions on one side and have a stereochemically active lone pair of electrons opposite. It is therefore somewhat surprising to discover that Sr²⁺ can substitute for Pb²⁺ to form SrMnBO₄ and Pb_{0.5}Sr_{0.5}MnBO₄ (and, presumably, all compositions in the solid solution Pb_{1-x}Sr_xMnBO₄). However, since Pb²⁺ and Sr²⁺ have almost

Table 4. Selected Bond Distances (Å) and Angles (°) for PbMnO₄, SrMnBO₄, Pb_{0.5}Sr_{0.5}MnBO₄, and Gaufreyite at 300 K

	PbMnBO ₄	SrMnBO ₄	Pb _{0.5} Sr _{0.5} MnBO ₄	Gaufreyite ^a
Mn–O2	1.985(2) [×2]	1.953(2) [×2]	1.943(3) [×2]	1.972(1)
Mn–O1	1.881(1) [×2]	1.846(2) [×2]	1.875(3) [×2]	1.870(1)
Mn–O3	2.212(2) [×2]	2.379(2) [×2]	2.338(6) [×2]	2.235(1)
α	83.8(1)	85.21(8)	85.4(2)	85.19(5)
β	84.8(2)	77.82(9)	79.4(2)	82.45(5)
γ	103.9(2)	108.1(2)	105.5(3)	103.90(7)
Pb–O1	2.423(6)		2.479(6)	
	2.342(5)		2.355(6)	
Pb–O2	2.434(3) [×2]		2.545(4) [×2]	
			2.777(5) [×2]	
Pb–O3	2.991(5)		2.678(7)	
Sr–O1		2.479(3)	2.479(6)	
		2.460(3)	2.355(6)	
Sr–O2		2.625(2) [×2]	2.545(4) [×2]	
		2.645(3) [×2]	2.777(5) [×2]	
Sr–O3		2.531(3)	2.678(7)	
Mn BVS	3.12	3.15	3.10	3.17
Pb BVS	1.90		2.06	
Sr BVS		2.09	2.09	

^aDerived from Hoffmann et al.¹⁶

identical ionic radii²⁷ and bond valence sums (BVS),²⁸ if adequate space for the lone pair is available, such a substitution is plausible, but the loss of the lone pair of electrons in SrMnBO₄ would inevitably result in a significant contraction in the unit cell. It is therefore important initially to consider the structural changes that occur when Pb²⁺ is replaced by Sr²⁺.

NPD data were collected at 300 and 1.5 K from all three compounds. The synthesis of pure samples of SrMnBO₄ had proven difficult, but the final sample used appeared pure from an XRPD refinement. However, two contaminants were detected in the NPD patterns: SrB₂O₄ (4 wt %) and Mn₂O₃ (3 wt %). These well-characterized impurities were therefore included as additional phases and caused no problems in the refinement; the other samples were phase pure. The refinements were straightforward without any constraints and allowed independent isotropic displacement parameters (IDPs) to be varied. Refinement suggested all sites to be fully occupied and they were therefore fixed at unity. The *Pnma* space group of PbMnBO₄ is retained in all samples, but there are major changes to the unit cell dimensions on substitution, as indicated by the refined structural parameters in Tables 1–3. The tables reveal only minor structural changes on cooling to 1.5 K. At 300 K, the unit cell volume of SrMnBO₄ (329.728(3) Å³) is 4% smaller than that of PbMnBO₄ (343.519(5) Å³), consistent with the loss of the lone pair of electrons. It is important to note, however, that the

full substitution of Sr causes little change in *b* (0.6% increase in the direction of the MnO₆ chains) but a large decrease in *a* (8%) and a substantial increase in *c* (4%). The major structural changes might therefore be expected to have a minor effect on magnetic exchange within the chains but are likely to influence the inter-chain properties significantly. The unit cell parameters for Pb_{0.5}Sr_{0.5}MnBO₄ are intermediate between those of the end members but are closer to those of SrMnBO₄.

Table 4 and Figure 2 provide detailed information to allow analysis of the structural differences between the three synthesized compounds. Table 4 provides bond distance and angle data relating to the MnO₆ chains (important for intra-chain magnetic interactions) and the Pb/Sr coordination; it also provides BVS information for these ions. Some data from the related mineral, gaufreyite, are also included. For all four compounds, we see that the MnO₆ octahedra show large Jahn-Teller distortions with the longest and shortest Mn–O bonds (to O3 and O1, respectively) being to the two O atoms in the linking edge. This will be considered later with respect to the intra-chain magnetic exchange. In PbMnO₄, Pb has four bonds to O, giving the common geometry with all O atoms on one side and consistent with the lone pair of electrons situated on the opposite side. Table 4 includes a 5th O which is significantly more distant from Pb but is included for the BVS calculation. Figure 2 shows that the lone pairs will be located in the space between adjacent Pb atoms. It is

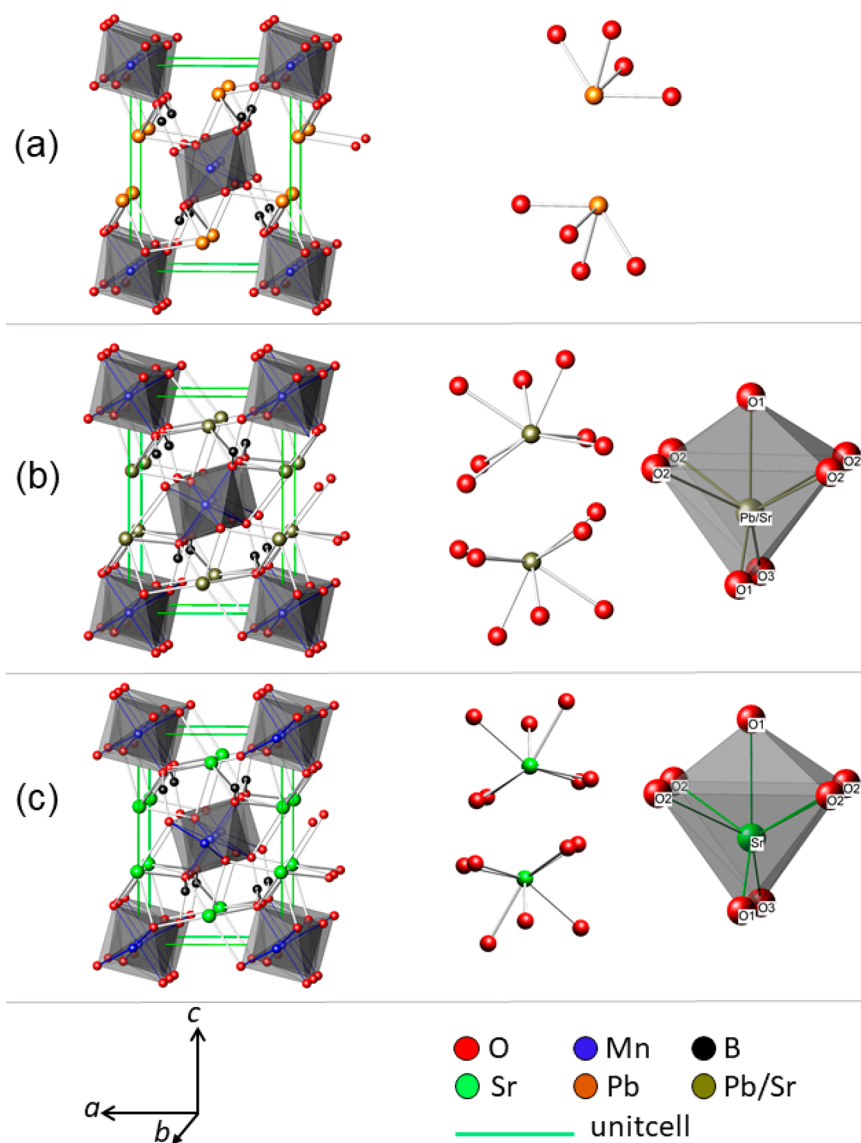


Figure 2. Structures and (Pb/Sr) coordination polyhedra for (a) PbMnBO_4 , (b) $\text{Pb}_{0.5}\text{Sr}_{0.5}\text{MnBO}_4$, and (c) SrMnBO_4 . The unit cell axes relate only to the full structures. The coordination polyhedra show the region between adjacent polyhedra and for (b) and (c) the solid polyhedra with capped trigonal prism (C_{2v}) geometry.

interesting that the coordination around the Pb/Sr cations in the other two compounds is quite similar with a coordination number of seven. Figure 2 shows that the O atoms are in a single-capped trigonal prism arrangement with the cap on a rectangular face of the prism (four O2 atoms). The changes in a and c unit cell distances relate to the preferred coordination of Pb^{2+} and Sr^{2+} ions. Figure 2 shows that in SrMnBO_4 , the Sr ions move to a more central position between the MnO_6 chains and, by attracting the chains towards it along a , can bond to seven O atoms in three different chains to achieve a more regular coordination than that of Pb in PbMnBO_4 . Comparison of Tables 1 and 3 shows large shifts along a for Sr (compared with Pb) and O3 to which Sr becomes bonded. The higher coordination number results in longer bonds which cause an expansion in the c direction. A similar geometry for the M^{2+} cations in both SrMnBO_4 and $\text{Pb}_{0.5}\text{Sr}_{0.5}\text{MnBO}_4$ shows that the coordination is acceptable for both cations and Figure 2b,c shows that pairs of (Pb/Sr) O_7 polyhedra exist with space between them to accommodate the Pb lone pair electrons. This coordination appears to be rare for Pb^{2+} , although a

similar PbO_7 polyhedron is found in $\text{Pb}_2\text{V}_3\text{O}_9$.²⁹ Tables 1–3 show that the Pb/Sr and O IDP values for $\text{Pb}_{0.5}\text{Sr}_{0.5}\text{MnBO}_4$ are generally larger than the end-member phases, which suggests slightly different atom positions in SrO_7 and PbO_7 polyhedra, but the differences are small and consistent with the almost identical BVS parameter for the two cations.²⁸ Table 4 shows BVS values for Mn^{3+} , Pb^{2+} , and Sr^{2+} which are close to their predicted values. The refinement plots for SrMnBO_4 at 300 K (122° detectors shown since their Q-range includes all low-Q peaks) are shown in Figure 3, and those for PbMnBO_4 and $\text{Pb}_{0.5}\text{Sr}_{0.5}\text{MnBO}_4$ are shown in the Supporting Information, Figures S1 and S2, respectively.

Given the significant structural differences between PbMnBO_4 and the Sr-containing phases, their magnetic properties were investigated by magnetometry and variable temperature NPD.

Magnetic Ordering: Magnetization and NPD Measurements. Plots of magnetic susceptibility (χ) and inverse susceptibility against temperature are shown in Figure 4 for the three samples. Qualitatively, the plots are similar and indicate a

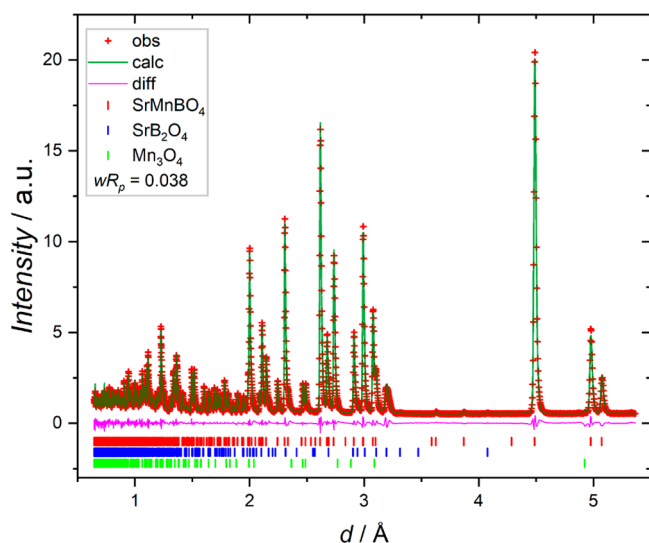


Figure 3. Rietveld refinement plots (122° detectors) for SrMnBO_4 at 300 K.

transition on cooling to a state which is either FM or has a FM component, e.g., canted AFM. The $\chi^{-1}(T)$ plots show deviations from Curie-Weiss (C-W) behavior below 150 K (PbMnBO_4), 200 K ($\text{Pb}_{0.5}\text{Sr}_{0.5}\text{MnBO}_4$), and 100 K (SrMnBO_4). Analysis of the data in the C-W regions is summarized in Table 5 with estimates of the transition temperatures (corresponding to initial major deviations in the $\chi^{-1}(T)$ plots) and C-W temperatures (θ).

The data for PbMnBO_4 are in agreement with those reported previously.¹⁹ It is seen that θ is positive for all compounds and indicates predominantly FM interactions in the C-W region. Impurities are unlikely to be responsible since $\text{Pb}_{0.5}\text{Sr}_{0.5}\text{MnBO}_4$ is phase pure. As was suggested for PbMnBO_4 ,¹⁹ the deviations from the C-W law at lower temperatures are consistent with the occurrence of short-range FM correlations, presumably within the MnO_6 chains. The effective magnetic moments, μ_{eff} are close to the spin-only value of $4.9 \mu_B$, and the lack of an orbital contribution is expected for the distorted octahedral environment for Mn^{3+} ions.

The nature of the magnetically ordered state was determined from the NPD data at 1.5 K. The magnetic scattering for PbMnBO_4 and SrMnBO_4 was initially compared by subtracting the observed profiles above the transition temperature (35 K for PbMnBO_4 and 20 K for SrMnBO_4) from those at 1.5 K. The results are shown in Figure 5. The main magnetic peaks for PbMnBO_4 , (101) and (002), are as previously reported¹⁹ and correspond with FM order both within the chains and between the chains with the moment directed along [100]; the magnetic space group is directly related to the nuclear space group and is $Pnm'a'$. However, Figure 5 clearly shows a (100) magnetic peak which has not previously been reported. Although forbidden for nuclear scattering by the a -glide plane, the reflection is allowed for the a' magnetic symmetry element. The observation of (100) allows retention of the propagation vector $k = (0,0,0)$ and suggests an AFM modulation along c (perpendicular to the FM moment) which provides in-phase scattering for (100) and is consistent with $Pnm'a'$ ($m\Gamma_3^+$ irreducible representation³⁰). No magnetic component along [010] was observed.

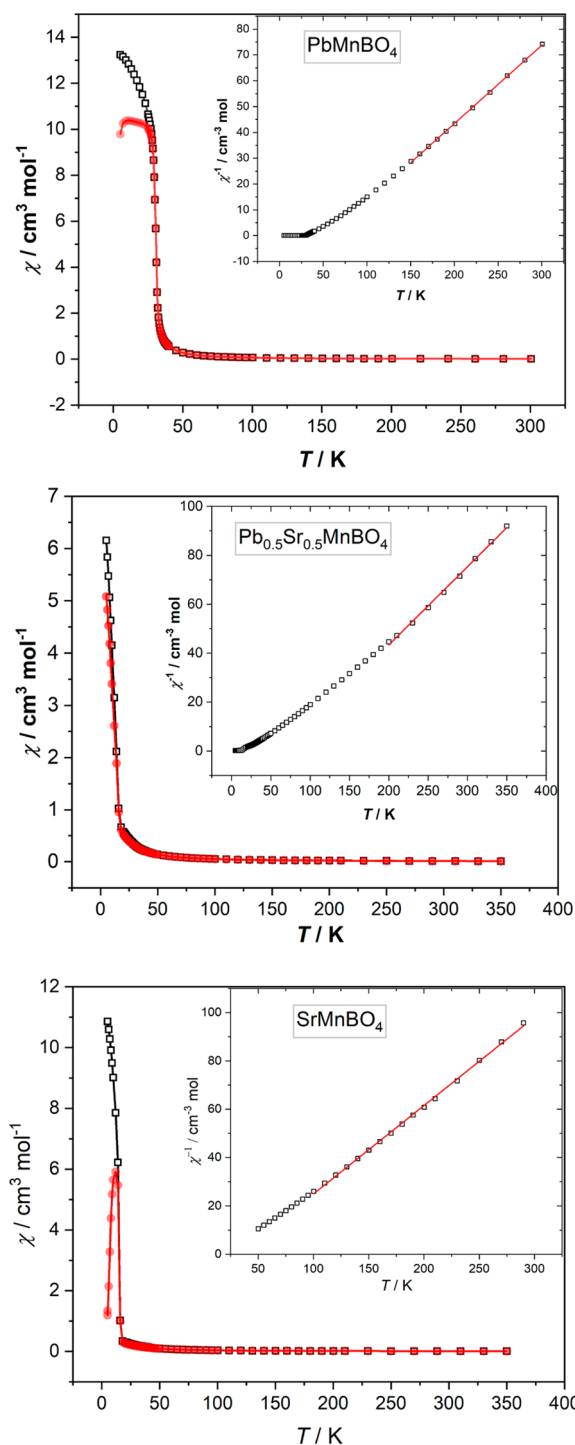


Figure 4. Plots of $\chi(T)$, with insets $\chi^{-1}(T)$, in an applied field $\mu_0 H = 10$ mT: ZFC red and FC black.

For SrMnBO_4 , the only dominant feature is the strong (001) reflection, which is also forbidden in $Pnma$ and suggests an inter-chain AFM arrangement of the FM chains with the moment within the ab plane. The only symmetry-allowed solution is for the moment to be aligned along [100] in $Pn'm'a$ ($m\Gamma_2^+$ irreducible representation³⁰). Given that the magnetization measurements indicate a FM component to the ordered state, it is relevant to note that $Pn'm'a$ allows canting to provide a FM moment only along [001]. $\text{Pb}_{0.5}\text{Sr}_{0.5}\text{MnBO}_4$ shows very similar magnetic features in its NPD pattern to

Table 5. Magnetic Parameters from Susceptibility Measurements

	ordering temperature	Curie constant (C)	$\mu_{\text{eff}}/\mu_{\text{B}}$	C-W temperature θ/K	temp range/K
PbMnBO ₄	$T_c = 30.0 \text{ K}$	3.30	5.1(1)	57(1)	150–300
SrMnBO ₄	$T_N = 16.1 \text{ K}$	2.73	4.7(1)	32(2)	100–300
Pb _{0.5} Sr _{0.5} MnBO ₄	$T_N = 16.0 \text{ K}$	3.13	5.0(1)	64(2)	200–350

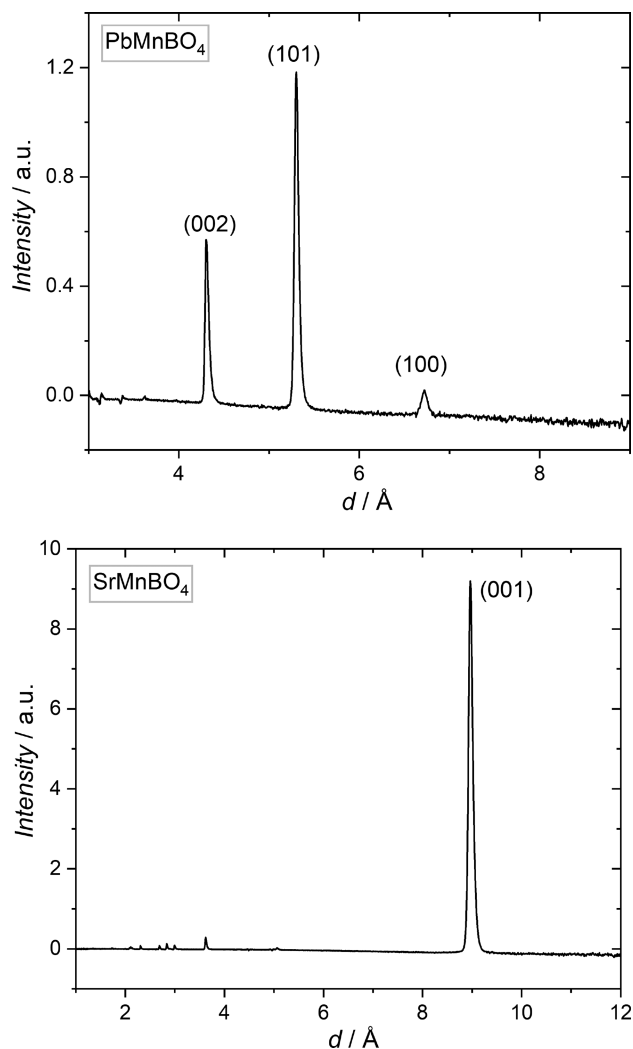


Figure 5. NPD profiles for $[I_{\text{obs}}(1.5 \text{ K}) - I_{\text{obs}}(35 \text{ K})]$ and $[I_{\text{obs}}(1.5 \text{ K}) - I_{\text{obs}}(20 \text{ K})]$ for PbMnBO₄ and SrMnBO₄, respectively.

SrMnBO₄, and the FM components to their susceptibilities (Figure 4) relate to this canting. The low temperature divergence between FC and ZFC data reflects different field dependencies for the FM component of SrMnBO₄ and Pb_{0.5}Sr_{0.5}MnBO₄, which is also apparent in the isothermal field sweep magnetization data (vide infra).

The magnetic models allowed straightforward NPD refinements of the basic magnetic structures and inclusion of the small AFM moment along [001] in PbMnBO₄ was also stable to give $\mu_z = 0.41(6) \mu_{\text{B}}$. The FM canting moments for the Sr-containing phases were too small to provide a significant effect and μ_z was constrained to zero. The final magnetic moments are $\mu_x = 3.42(4) \mu_{\text{B}}$, $\mu_y = 0 \mu_{\text{B}}$, $\mu_z = 0.41(6) \mu_{\text{B}}$, and $\mu_{\text{total}} = 3.44(4) \mu_{\text{B}}$ for PbMnBO₄; $\mu_x = 3.71(1) \mu_{\text{B}}$, $\mu_y = 0 \mu_{\text{B}}$, $\mu_z = 0.0 \mu_{\text{B}}$, and $\mu_{\text{total}} = 3.71(1) \mu_{\text{B}}$ for Pb_{0.5}Sr_{0.5}MnBO₄; and $\mu_x = 3.42(4) \mu_{\text{B}}$, $\mu_y = 0 \mu_{\text{B}}$, $\mu_z = 0.0 \mu_{\text{B}}$, and $\mu_{\text{total}} = 3.42(4) \mu_{\text{B}}$ for SrMnBO₄. These data are also provided in Tables 1–3. The

moments are $\sim 10\%$ below the expected $4.0 \mu_{\text{B}}$ which can be attributed primarily to covalence. Figure 6 shows Rietveld refinement plots for all samples against data for detectors which include all of the lowest-Q magnetic reflections. Figure 7

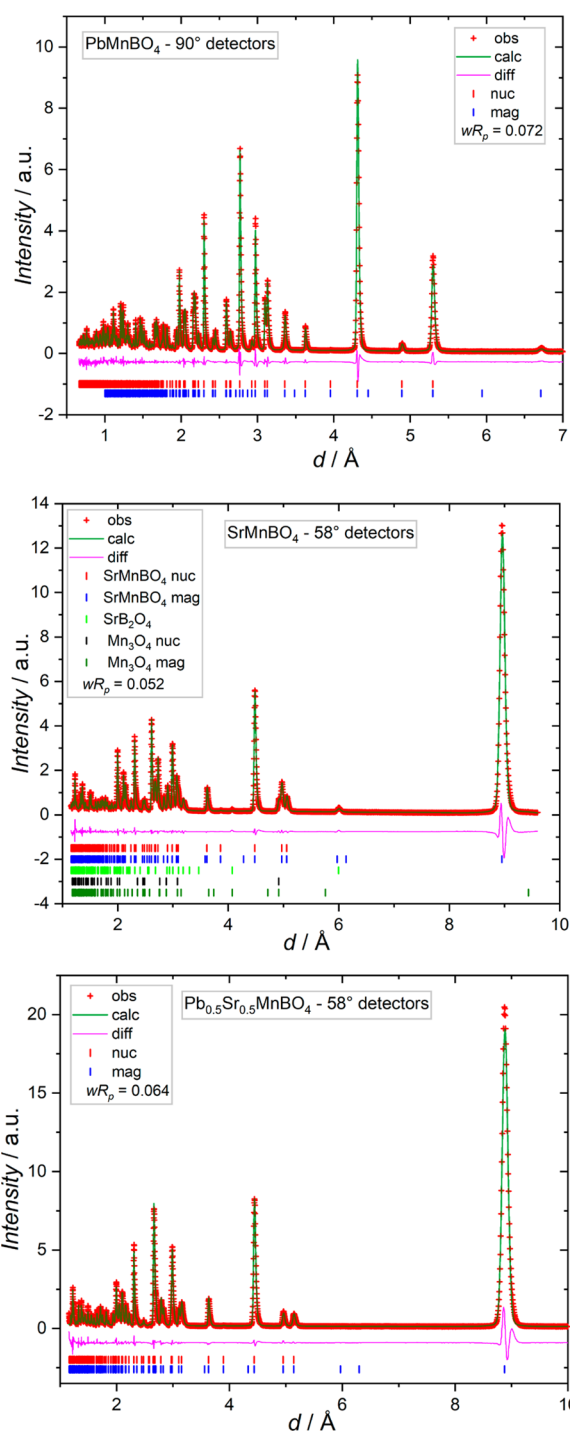


Figure 6. Rietveld refinement plots for samples at 1.5 K.

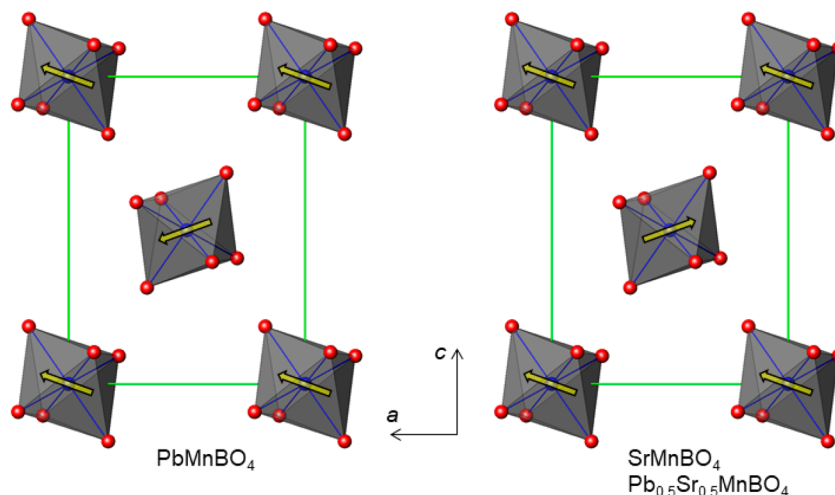


Figure 7. Schematic comparison of the FM and AFM order in PbMnBO_4 , SrMnBO_4 , and $\text{Pb}_{0.5}\text{Sr}_{0.5}\text{MnBO}_4$. The canting of the moments is exaggerated for clarity.

gives a schematic representation (the deviation of the moments from the a -axis are exaggerated) of the two magnetic arrangements viewed along $[010]$, the direction of the MnO_6 chains. In both, the moments are purely FM within each chain.

The variation of magnetic scattering between 1.5 K and the magnetic ordering temperatures were determined by the changes in magnetic peak intensities: the (001) purely magnetic peak for SrMnBO_4 and $\text{Pb}_{0.5}\text{Sr}_{0.5}\text{MnBO}_4$ and (101) for PbMnBO_4 . The latter peak was corrected for the small amount of nuclear intensity. Figure 8 focuses on the variation

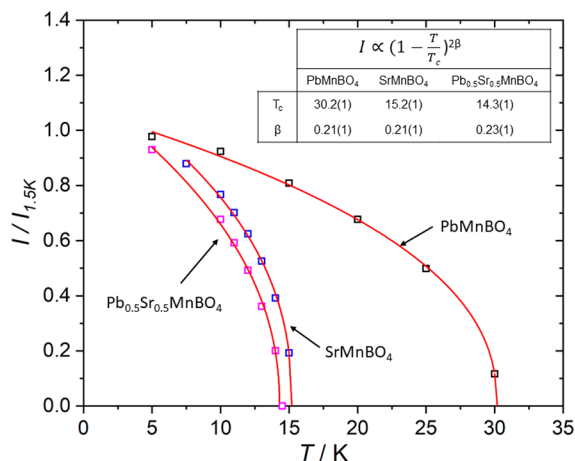


Figure 8. Fits of magnetic peak intensity against T for the mean field scaling $I \propto (1 - \frac{T}{T_c})^{2\beta}$.

of peak intensities with temperature near to the ordering temperature (here represented by T_c), where good compliance is expected with the mean field scaling equation

$$I \propto (1 - \frac{T}{T_c})^{2\beta}$$

The fitted parameters, β and T_c , are given in the inset to Figure 8; the ordering temperatures are in reasonable agreement with the data from magnetization measurements (Table 5) but are more precise. Although the experimental data are limited, the values of β for PbMnBO_4 (0.21(1)), SrMnBO_4 (0.21(1)), and $\text{Pb}_{0.5}\text{Sr}_{0.5}\text{MnBO}_4$ (0.23(1)) are very similar and consistent with that reported for

gaudfroyite (0.20(2)).¹⁸ They are typical of low dimensional magnetically ordered materials.^{31,32}

To explore the canting of the moments in the AFM Sr-containing phases, isothermal field sweep magnetization measurements were performed at 10 K, and the results for all three samples are shown in Figure 9. PbMnBO_4 shows simple FM behavior with a small coercivity of ~ 35 mT, whereas SrMnBO_4 and $\text{Pb}_{0.5}\text{Sr}_{0.5}\text{MnBO}_4$ show a FM hysteresis loop at low field followed by a gradually increasing moment at higher fields. The FM component confirms a canted AFM ground state; the form of the hysteresis loops and remanent magnetization values suggest canting moments of $0.21 \mu_B$ for SrMnBO_4 and $0.07 \mu_B$ for $\text{Pb}_{0.5}\text{Sr}_{0.5}\text{MnBO}_4$ along $[001]$. Such small FM components would be very difficult to detect in our NPD experiments.

Magnetostriction and Magnetic Exchange Interactions. Careful monitoring of the unit cell dimensions during heating and cooling revealed significant changes for PbMnBO_4 and SrMnBO_4 at their magnetic phase transitions as shown in Figure 10. No clear evidence for this spontaneous magnetostriction was found for $\text{Pb}_{0.5}\text{Sr}_{0.5}\text{MnBO}_4$. The changes observed are larger for PbMnBO_4 (FM inter-chain exchange) than SrMnBO_4 (AFM inter-chain exchange). Defining the magnetostriction constant for a as $\lambda_{100} = (a_{1.5K} - a')/a'$ (where a' applies to just above the ordering temperature) etc., then for PbMnBO_4 , $\lambda_{100} = 3.0 \times 10^{-4}$, $\lambda_{010} = 3.0 \times 10^{-4}$, $\lambda_{001} = -3.0 \times 10^{-4}$, and $\lambda_{\text{vol}} = 3.0 \times 10^{-4}$ and for SrMnBO_4 $\lambda_{100} = 0.4 \times 10^{-4}$, $\lambda_{010} = 0.7 \times 10^{-4}$, $\lambda_{001} = 0.8 \times 10^{-4}$, and $\lambda_{\text{vol}} = 2.0 \times 10^{-4}$. The structural changes reflect the effects of structural strains associated with ordering of the magnetic moments, and significant magnetostriction is usually linked with magneto-crystalline anisotropy which here will be provided by the large Mn^{3+} Jahn-Teller distortion.^{33,34} All constants indicate expansion on cooling through T_c/T_N except for λ_{001} for PbMnBO_4 . Unfortunately, it is difficult to analyse the details of the magnetostriction because no significant change to structural parameters are suggested by the NPD refinements except for the changes in unit cell size. The opposing signs of λ_{001} for PbMnBO_4 and SrMnBO_4 probably relate to the switch between FM and AFM inter-chain order. We also see that the changes in dimensions for SrMnBO_4 are very sharp except for b , whereas PbMnBO_4 shows more gradual changes especially for the b -axis. The expansion along $[010]$ appears similar in

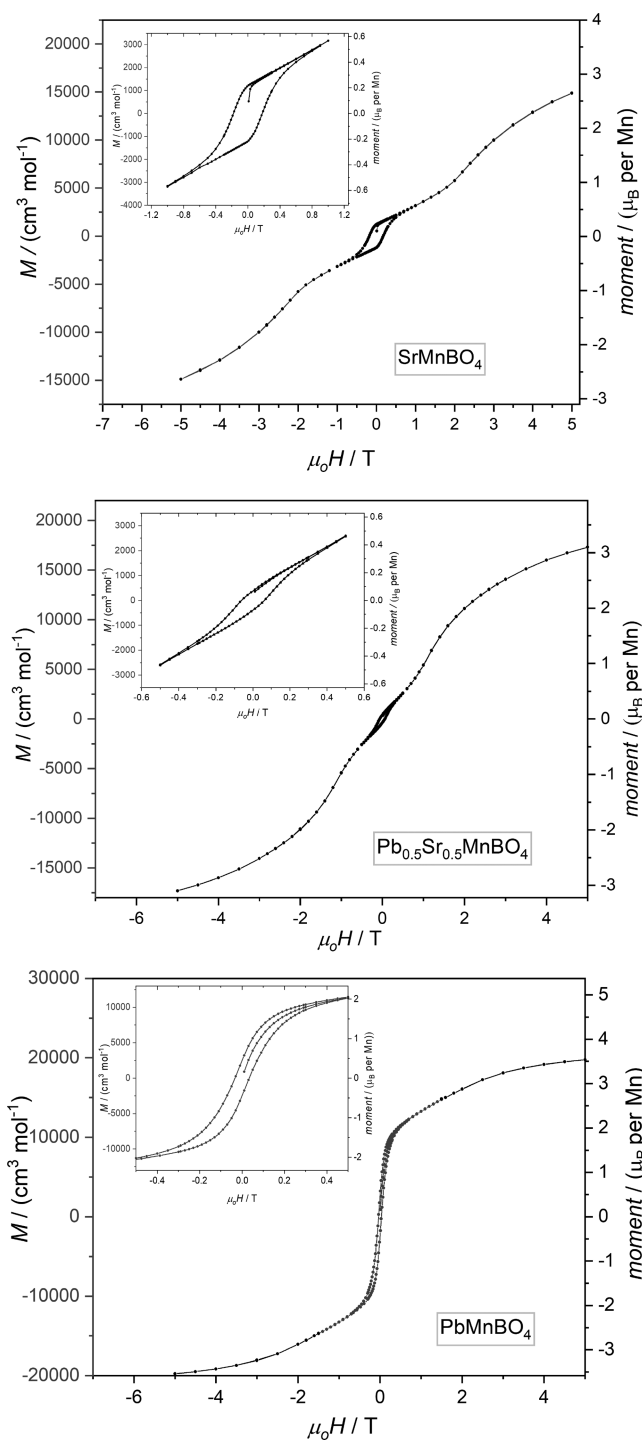


Figure 9. Magnetization vs applied field at 10 K for SrMnBO₄, Pb_{0.5}Sr_{0.5}MnBO₄, and PbMnBO₄.

both phases, and the strain is probably dominated by the common FM chains of MnO₆ octahedra in this direction. Significantly, the results suggest that structural strain is occurring in the direction of the chains at temperatures significantly above that for 3D order; this is marked for PbMnBO₄ and is supportive of short-range FM order within the chains for $T > T_c$. It is also interesting to note that the spontaneous increase in a and decrease in c that occur in PbMnBO₄ on cooling through T_c continues the trend seen when Pb is substituted for Sr in AFM SrMnBO₄ ($a =$

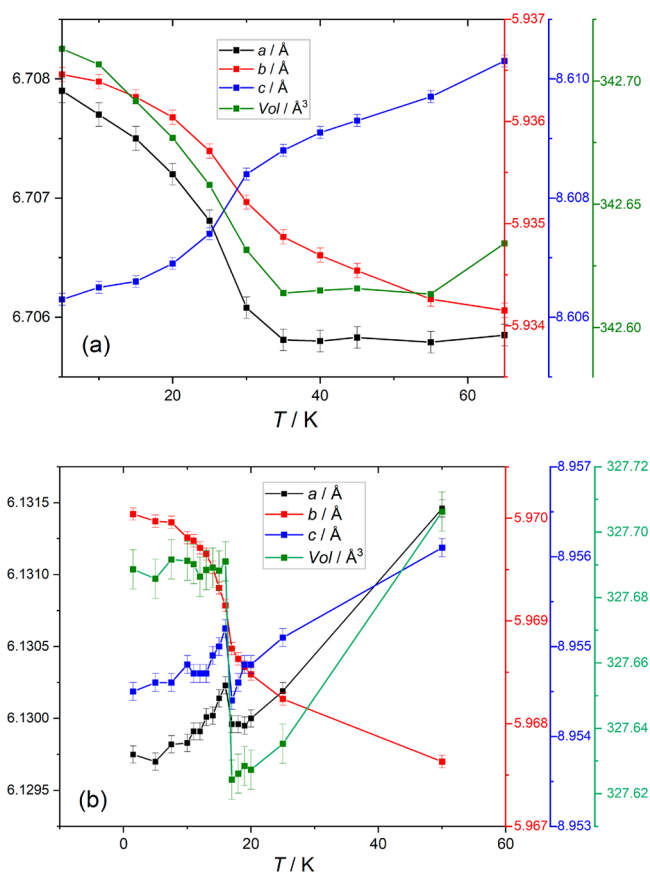


Figure 10. Variation of unit cell dimensions with T for (a) PbMnBO₄ and (b) SrMnBO₄. The plots are color-coded to the y-axis scales.

6.14892(3) Å and $c = 8.97067(6)$ Å) to form PbMnBO₄ ($a = 6.69380(5)$ Å and $c = 8.63691(7)$ Å) with dominant FM inter-chain magnetic exchange. It is therefore likely that the magnetostriction provides additional stabilization of the inter-chain FM ground state in PbMnBO₄.

The magnetostriction behavior of PbMnBO₄ and SrMnBO₄ reflects the similarities and differences between the magnetic exchange interactions in these structurally related materials. Both phases display intra-chain FM behavior in accordance with the predictions based on the Goodenough–Kanamori–Anderson (GKA) rules^{35–37} for $\sim 90^\circ$ M–O–M (M = transition metal) links and the detailed information in Table 4. For a d^4 high-spin cation (e.g., Mn³⁺), an M–O–M link will provide AFM exchange when the O is bonded to empty (d^0) and half-full (d^1) orbitals and FM for $d^0 \cdots d^0$ and $d^1 \cdots d^1$. For all samples under current investigations, Table 4 shows that the long Mn–O3–Mn bonds involve the singly-occupied Mn d_z^2 orbitals and the shorter Mn–O1–Mn bonds are formed by the empty $d_{x^2-y^2}$ orbital; hence all bonds linking Mn in the chains give FM exchange between neighboring Mn ions. Although the mechanism relies on relatively weak electron exchange interactions to maximize the unpaired electron spin on the orthogonal 2p orbitals on O1 and O3, this will be the primary basis for the intra-chain FM behavior. But what causes the change from FM inter-chain exchange in PbMnBO₄ to AFM exchange in SrMnBO₄? In Figures 11 and 12 we explore the relevant structural differences and their possible magnetic consequences.

Figure 11a shows the structure of PbMnBO₄ highlighting the most obvious magnetic pathway between the closest FM

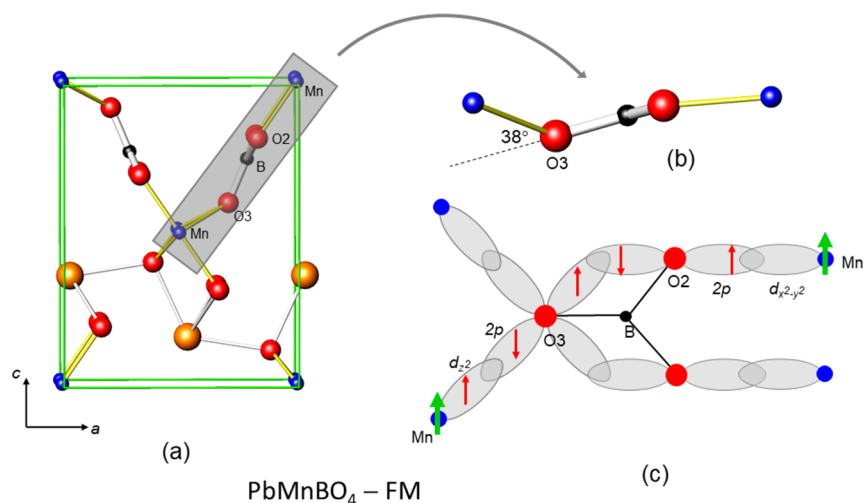


Figure 11. (a) Structure of PbMnBO₄ viewed along the chains ([010]) highlighting the borate links; (b) an enlargement of the almost planar Mn–O₃–B–O₂–Mn link; (c) a schematic viewed perpendicular to the BO₃ group to show a FM exchange mechanism. In panel c, the electron moments are red and the overall chain moments are green (see the text).

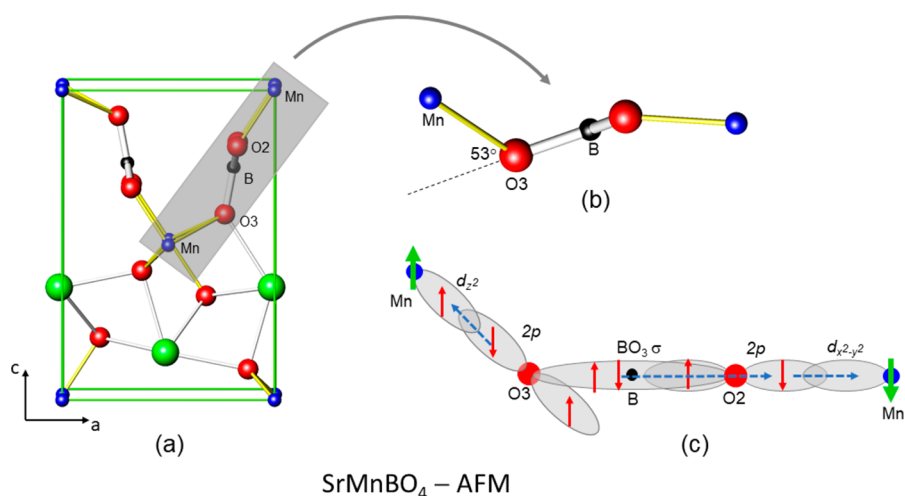


Figure 12. (a) Structure of SrMnBO₄ viewed along the chains ([010]) highlighting the borate links; (b) an enlargement of a link showing the large angle between the plane of the BO₃ group and the bonds between Mn and O₃; (c) a schematic view along panel b to show an AFM interaction via an electron exchange energy mechanism. In panel c, the electron moments are red, the overall chain moments are green, and the small blue dashed arrows on the moments indicate movements and interactions (see the text). The scheme assumes the link is via the BO₃ σ -orbital.

chains; this involves the borate group and the link is enlarged in Figure 11b. The linkage is quite flat (Figure 11b) although the figure shows that the Mn ions bonded to O₃ are out-of-plane. If we assume that the O 2p-orbitals are directed towards the Mn ions, as is normal for 90° exchange (vide supra) then they cannot contribute significantly to the BO₃ σ -orbital as illustrated in Figure 11c, which shows the relevant orbitals viewed perpendicular to the plane of the borate group. The BO₃ σ -orbital may primarily be derived from the O 2s orbitals, but this is not important for the current discussion. The GKA rules^{35–37} may be applied to several combinations of atomic/molecular orbitals to provide FM superexchange (SE) interaction between the Mn ions via the BO₃ groups. However, Figure 11c highlights that a super-superexchange (SSE) mechanism should also be considered and would comprise the Mn···O₃···O₂···Mn interaction where O₃ and O₂ form an edge of the borate group.

This mechanism can be stronger than simple SE and is favored by large Mn–O₃–O₂ and Mn–O₂–O₃ angles and a

short O–O distance.^{38,39} The covalent bonding in BO₃ results in a very short O–O distance (2.38 Å) which is ideal for orbital overlap. The Mn–O–O angles for PbMnBO₄ are 148° and 155° which should also provide suitable orbital overlap. We therefore favor this fairly simple SSE exchange mechanism for PbMnBO₄; it is illustrated in Figure 11(c) for one link between the occupied d_{z^2} orbital of a Mn ion in one chain and the empty $d_{x^2-y^2}$ orbital of a Mn in an adjacent chain.

In SrMnBO₄, we seek a different mechanism that can rationalize the AFM inter-chain exchange – the Mn ions bonded to O₃ are now moved further away from the plane containing the BO₃ group as seen in Figure 12a,b. The angle shown as 38° for PbMnBO₄ (Figure 11b) is now 53° for SrMnBO₄ and the Mn–O–O angles that are 148° and 155° for PbMnBO₄ are reduced to 136° and 149°. The 2p orbitals on O₃ are now unsuitable for involvement in the BO₃ σ -orbital or any π -bonding in the borate group. The FM SSE pathway now appears too weak, which is supported by the fact that the angle of 38° for PbMnBO₄ (Figure 11b) is 53°, 53°, and 47°

for the three phases with AFM inter-chain interactions, SrMnBO₄, gaufreyite, and Pb_{0.5}Sr_{0.5}MnBO₄, respectively. We propose a mechanism based on electron exchange energy considerations for these phases and illustrated in Figure 12c. This mechanism, the basis of Hund's rules, relies on second-order perturbation theory; it is therefore usually quite weak but provides the FM coupling in the 90° Mn–O–Mn intra-chain interactions. In simple terms (and represented in Figure 12(c)), the excess spin-up density on O3 resulting from partial transfer of a spin-down electron to the Mn d_{z²} orbital allows stabilization when there exists spin-up for unpaired electrons in the BO₃ σ-orbital and also in the 2p orbital on O2. This is achieved by transfer of spin-down electron to the Mn d_{x²-y²} orbital and gives overall AFM interaction. The weakness of this exchange explains why T_N for SrMnBO₄ and Pb_{0.5}Sr_{0.5}MnBO₄ is ~16 K compared with T_c ≈ 30 K for PbMnBO₄ with FM inter-chain links.

Only subtle structural effects differentiate between the proposed inter-chain exchange mechanisms for FM PbMnBO₄ and AFM SrMnBO₄. These mechanisms are specific to the observed orbital order in the Jahn-Teller stabilized Mn³⁺ ions, and it is relevant to note that PbCrMnO₄ and PbFeBO₄ show FM inter-chain interactions. In fact, for the Cr³⁺ and Fe³⁺ electron configurations, the mechanism outlined for SrMnBO₄ would account for FM order between the chains in these compounds.

Neutron Powder Diffraction with Applied Field. In order to examine the effects of magnetic field on magnetic structure, NPD data were collected at various fields and temperatures for PbMnBO₄ and SrMnBO₄ samples. An unavoidable problem for polycrystalline samples is that crystallites will experience fields in different directions. To ensure a random distribution of crystal orientations, sintered pellets were used with crystals spatially locked even in magnetic fields. Unless there is a highly dominant easy magnetization axis, for orthorhombic structures with orthogonal axes, an applied magnetic field averaged over all crystals should introduce magnetic moments with equal components along the three Cartesian axes consistent with the magnetic unit cell, i.e., $m_x = m_y = m_z$. This was checked by comparing the field-induced magnetic neutron scattering in paramagnetic PbMnBO₄ with simulated magnetic diffraction profiles. For PbMnBO₄ at 35 K (in the paramagnetic region), the difference between the diffraction profiles in 4 and 0 T is shown in Figure 13a. Simulations of profiles for moments in various orientations revealed only two that could possibly be consistent with the observed scattering: those with moments along [010] (Figure 13b) or along [111]_m (Figure 13c). The subscript "m" (as in [111]_m) will be used to indicate a magnetic moment vector [xyz]_m referred to Cartesian axes; the direction does not coincide with the structural vector [xyz] and, although [100] ≡ [100]_m, [111]_m is not perpendicular to the (111) planes. It is seen that both models provide major scattering in the (101) and (002) reflections at $d \approx 5.3$ and 4.3 Å, respectively. The difference between the two possibilities is observed at shorter d -spacings: at ~2.6 and ~3.0 Å, the experimental scattering is reproduced only with moments along [111]_m. Obtaining the profile shown in Figure 13a proved important since these critical low intensity peaks are masked by nuclear scattering in Rietveld refinements. Rietveld refinement residuals, however, fully supported constraining the moments to the [111]_m direction. The Rietveld refinement plots at 35 K in 4 T are shown in Figure S3. The [111]_m

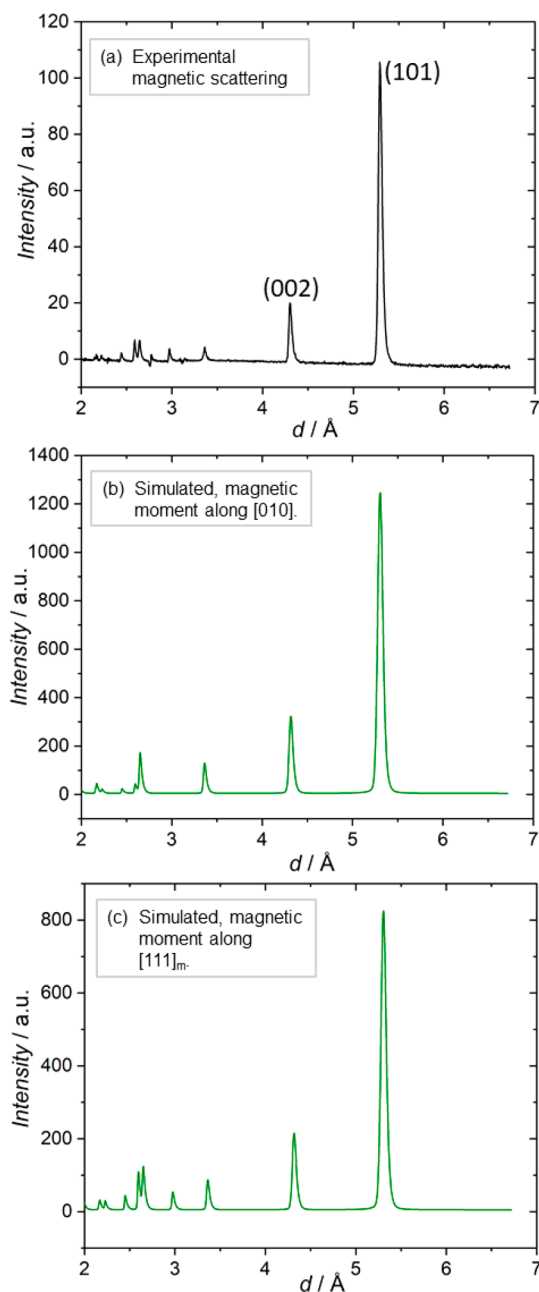


Figure 13. (a) NPD difference profile for PbMnBO₄: 4–0 T collected at 35 K; (b) simulated NPD pattern for moments aligned along [010]; (c) simulated NPD pattern for moments aligned along [111]_m.

direction for the induced moment was found to be true for SrMnBO₄ also, and all subsequent analysis of data obtained in applied fields was consistent with this orientation. The effects of magnetic fields both below and above T_c/T_N were examined for PbMnBO₄ and SrMnBO₄.

The effects of an applied magnetic field on the direction and magnitude of the principal FM moment in PbMnBO₄ at 1.5 K are shown in Figure 14. It is seen that the moment gradually rotates from being aligned along the *a*-axis to a direction with equal components along all three axes. This direction makes an angle of 54.7° with *a*, and we see that saturation occurs at ~3 T with a moment of 4.0 μ_B, in agreement with that expected for Mn³⁺ with no orbital contribution to the moment. For SrMnBO₄, with opposed moments along *a*, it is not straightforward to monitor exactly the change in moment as

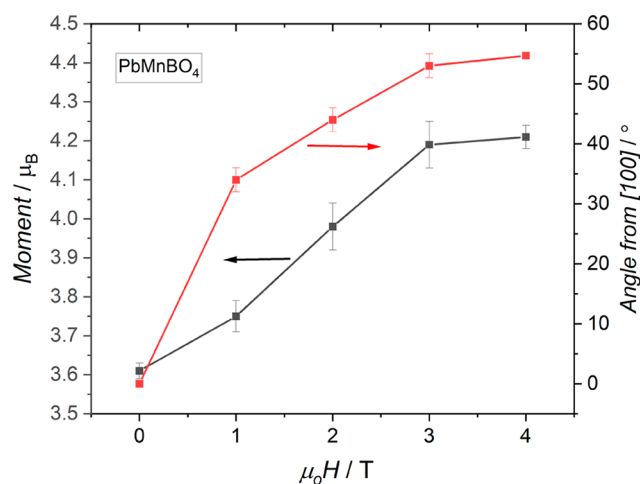


Figure 14. Variation of magnitude and direction of the FM magnetic moment with applied field in PbMnBO_4 at 1.5 K.

a function of applied field. However, the very large, totally magnetic (001) diffraction peak gives us a precise measure of the change in the AFM component with applied field. Data for 1.5 K are presented in Figure 15, which shows that the AFM

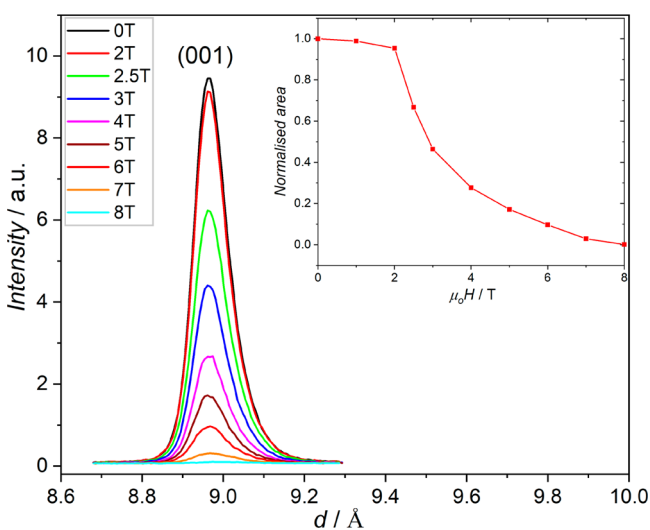


Figure 15. Change in intensity of the AFM (001) peak in SrMnBO_4 as a function of applied field at 1.5 K. The inset shows the change in integrated area with B .

order is not disrupted at fields up to ~ 2 T, and the diffraction peak then decreases quite smoothly with field; however, the AFM order disappears completely only at 8 T. The build-up of FM order was explored using Rietveld refinements by assuming that the applied field introduces a FM moment, which can be resolved equally along the three axes (along $[111]_m$). This can then be modeled by using two magnetic phases: one AFM which will decrease with field and a FM phase with equal components m_x , m_y , and m_z that increases with field. In the refinements, because of the correlation between magnetic moment and phase fraction, the phase fractions of the two components were fixed at 1.0, but the moments were varied and allowed calculation of the separate moments for each phase and hence the total ordered moment as shown in Figure 16. This figure also includes data for the AFM moment calculated from the (001) peak areas shown in

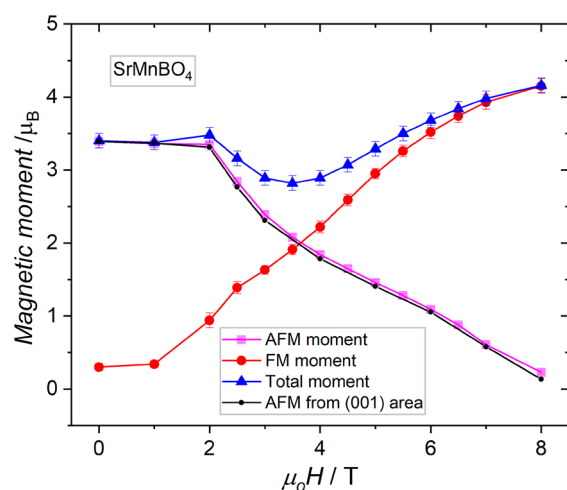


Figure 16. AFM (along $[100]$) and FM (along $[111]$) contributions to the overall ordered moment in SrMnBO_4 as a function of applied field at 1.5 K from Rietveld refinements. The AFM moment is compared with that from normalising the (001) peak area of Figure 15.

Figure 15. Since the peak area is proportional to m^2 , the normalized moment (m_o) was obtained from $m_o = 3.39 \times \sqrt{A/A_o}$ where A is the peak area and A_o the area at 1.5 K. The complete agreement between the two estimates of the AFM moment give confidence that the data in Figure 16 are a good representation of the magnetic changes occurring. It is seen that applied fields of $\mu_0 H \leq 2$ T fail to overcome the AFM exchange energy but at higher fields, the FM component increases until saturation occurs, but only at 8 T. At this field the FM moment is in the $[111]_m$ direction because of powder averaging, as was seen for PbMnBO_4 . SrMnBO_4 is therefore significantly less sensitive to the applied field than PbMnBO_4 where saturation is achieved at 3 T. The saturated moment in SrMnBO_4 is determined as $4.1(1) \mu_B$. The model used suggests that, for fields in the range 2–5 T, the total ordered magnetic moment is smaller than expected (Figure 16) and is indicative of some magnetic disorder in these intermediate fields because of the opposing interactions of the AFM exchange energy and the applied field direction. Representative NPD Rietveld refinement plots at intermediate applied magnetic fields are shown in Figure S4 (PbMnBO_4 at 2 T) and S5 (SrMnBO_4 at 4.5 T). It is important to note that the behavior of SrMnBO_4 (AFM inter-chain exchange) is very different from that of gaufreyite (frustrated AFM with 120° between the ordered moments), which at 100 mK becomes 90% FM in a field of 1 T and saturates at 3 T.¹⁷ Although this may predict inferior MCE behavior for SrMnBO_4 , the behavior near and above T_N is more important; variable field NPD data were therefore collected for PbMnBO_4 and SrMnBO_4 in the paramagnetic region.

Figure 17 shows the variation of the total FM moment with applied magnetic field for PbMnBO_4 and SrMnBO_4 at temperatures above T_c and T_N , respectively. It is seen that, at respective temperatures of 35 and 20 K (~ 5 K above the ordering temperatures), the moment of PbMnBO_4 is 57% saturated at 2 T and 74% at 4 T; at the same fields, SrMnBO_4 is only 26% and 51% saturated.

In comparison, gaufreyite at 15 K (again ~ 5 K above T_N) is 75% saturated at 3 T.¹⁷ This suggests that PbMnBO_4 could display very good MCE behavior at temperatures of ~ 30 K and

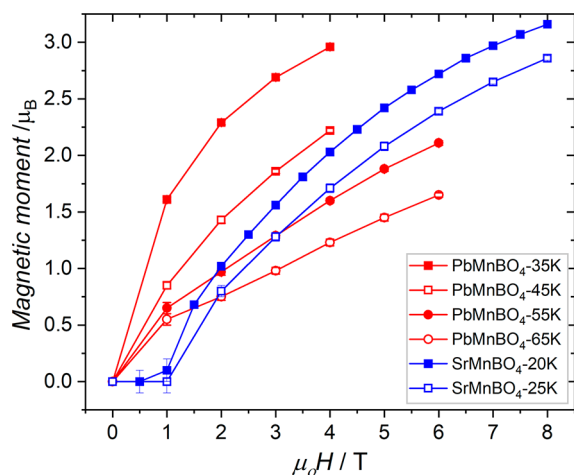


Figure 17. Variation of the FM magnetic moment induced by applied fields above the ordering temperatures of PbMnBO_4 and SrMnBO_4 .

above, but SrMnBO_4 would be expected to be less exciting. However, the lower magnetic ordering temperature for SrMnBO_4 may prove useful at the boiling point of hydrogen. The MCE properties of all three samples were therefore measured indirectly using magnetization data.

Magnetocaloric Properties. The magnetic entropy changes for applied fields up to 7 T were determined for all three samples as described in the **Experimental Methods** section, and the results shown in **Figure 18** refer conventionally to 1 kg of sample. All samples give a maximum in entropy change at a temperature slightly above that of the ordering temperature. In high fields, all three samples show similar values for the maximum $-\Delta S$, e.g., $\sim 6 \text{ J kg}^{-1} \text{ K}^{-1}$ at 6 T. At lower fields, PbMnBO_4 shows less reduction than the other samples probably because the field does not have to overcome an AFM exchange energy. We also see that above T_N/T_C , $-\Delta S$ decreases relatively slowly which is consistent with there being a significant field response in agreement with the presence of short-range FM order within the chains of MnO_6 octahedra in all compounds. The entropy changes are excellent for this temperature range where very few materials exhibit high MCE characteristics. The best proven material for operation at 20 K, needed for hydrogen liquefaction, is gaufreyite,¹⁷ and **Figure 19a** gives comparative data for this material and those described here at a low field (2 T) and a high field (6 T). It is clear that gaufreyite has superior properties at low temperatures, including 20 K. However, data for this mineral were collected from a single crystal with easy-axis orientation, and powder-averaging to allow more direct comparison would decrease the $-\Delta S$ values by $\sim 20\%$. For $T > \sim 25 \text{ K}$, it appears that even at 2 T PbMnBO_4 performs better than gaufreyite. More realistic comparisons can be made using data normalized on the $-\Delta S$ per mol Mn rather than per kg, and these are shown in **Figure 19**. We see that the mass of Pb plays an important role in determining the MCE performance and, allowing for the fact that PbMnBO_4 is in polycrystalline form, $-\Delta S_{\text{max}}$ values for both 2 T and 6 T appear very similar for PbMnBO_4 and gaufreyite. SrMnBO_4 and $\text{Pb}_{0.5}\text{Sr}_{0.5}\text{MnBO}_4$ are inferior at 2 T but good at 6 T. In fact, at high field the solid solution $\text{Pb}_{1-x}\text{Sr}_x\text{MnBO}_4$ has very good MCE behavior over the extended temperature range $15 \text{ K} < T < 40 \text{ K}$. The comparable behavior of gaufreyite and PbMnBO_4 near their Curie temperatures suggests that the magnetic frustration

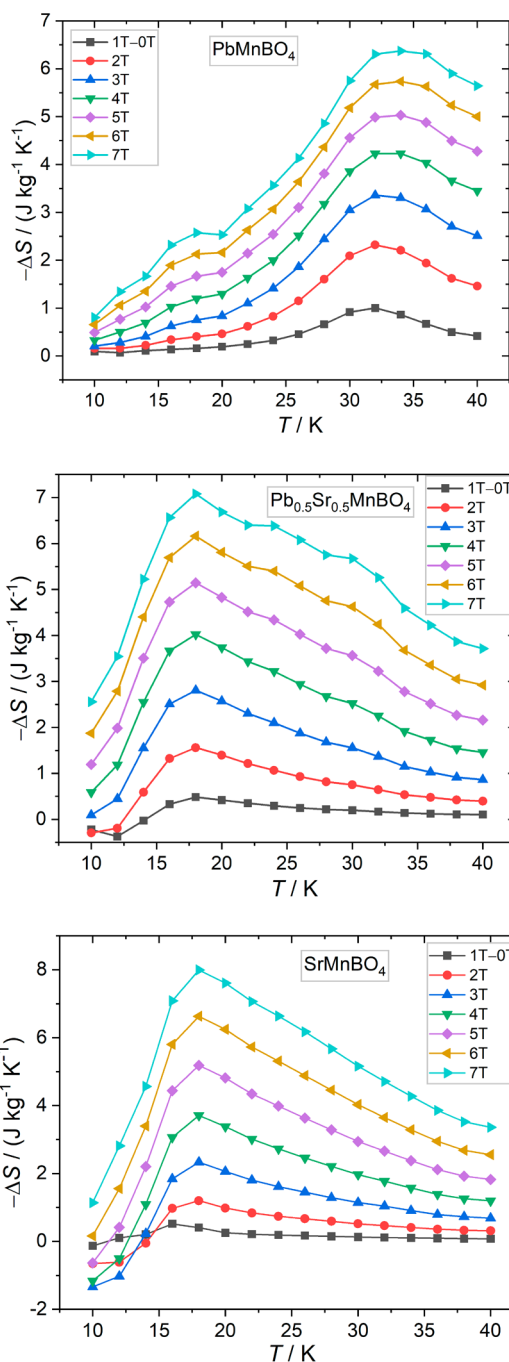


Figure 18. Magnetic entropy changes in PbMnBO_4 , $\text{Pb}_{0.5}\text{Sr}_{0.5}\text{MnBO}_4$, and SrMnBO_4 when switching from zero to various applied fields.

perpendicular to the MnO_6 chains in gaufreyite is not essential for the provision of excellent MC properties, but a large difference between the intra-chain and inter-chain magnetic exchange energies is needed. In fact, since we ideally need a magnetic ordering temperature of $\sim 20 \text{ K}$ for hydrogen liquefaction applications, this will be too high for highly frustrated materials.

CONCLUSIONS

The structures, both nuclear and magnetic, of PbMnBO_4 , SrMnBO_4 , and $\text{Pb}_{0.5}\text{Sr}_{0.5}\text{MnBO}_4$ have been determined to explore their applicability for MC cooling at temperatures suitable for hydrogen liquefaction, 20 K. PbMnBO_4 is FM with

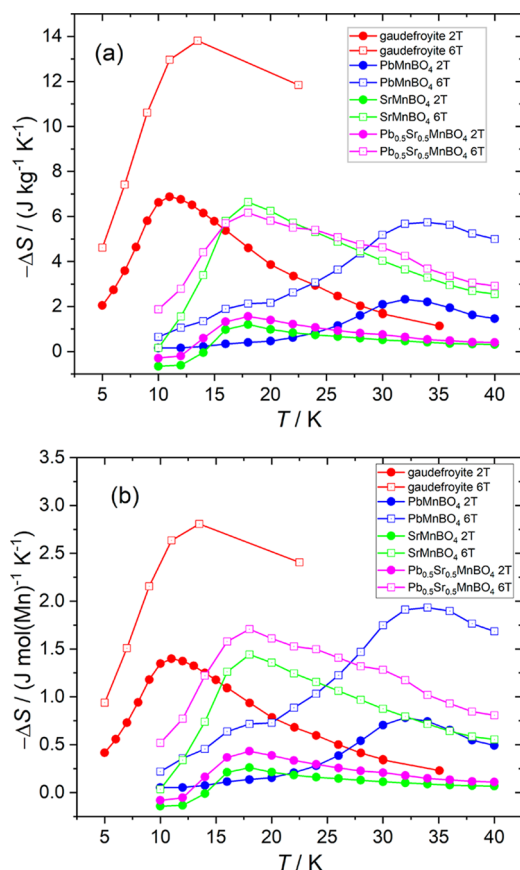


Figure 19. Comparison of magnetic entropy changes between 0–2 T and 0–6 T for gaufreyite,¹⁷ PbMnBO_4 , SrMnBO_4 , and $\text{Pb}_{0.5}\text{Sr}_{0.5}\text{MnBO}_4$ (a) per kg sample and (b) per mol Mn.

a small AFM contribution, whereas SrMnBO_4 and $\text{Pb}_{0.5}\text{Sr}_{0.5}\text{MnBO}_4$ display canted AFM magnetic order with lower magnetic ordering temperatures. All materials have strong FM coupling within the chains of MnO_6 octahedra and this relates primarily to the 90° Mn–O–Mn exchange interactions. The difference in inter-chain coupling is attributed to differences in the links which involve the BO_3 groups and rationalization of the switch from FM to AFM is possible. Exchange magnetostriction is observable for PbMnBO_4 and SrMnBO_4 and to some extent can be related to the different exchange interactions in these compounds. The broad magnetostriction along $[010]$, the chain direction, is consistent with short-range FM order existing within the chains above the magnetic ordering temperatures. The change of magnetic properties when subjected to applied magnetic fields was focused on the ability of these materials to exhibit useful MCE behavior at temperatures of ~ 20 K, necessary for liquefaction of hydrogen but higher than can be achieved for existing well-characterized materials. The magnetic properties showed that, for SrMnBO_4 and $\text{Pb}_{0.5}\text{Sr}_{0.5}\text{MnBO}_4$, low fields had little effect on the magnetic properties, presumably because of the inhibition caused by the energy to disrupt the inter-chain AFM order. In contrast, PbMnBO_4 seemed more sensitive to fields both below and above T_c . This was confirmed in calculations of $-\Delta S$, the change in magnetic entropy on removal of an applied field. In particular, PbMnBO_4 has excellent MCE behavior between 25 and 40 K, similar to that reported for alloys,⁸ but unfortunately too high for liquefying hydrogen; nevertheless, PbMnBO_4 and

related materials could be of interest for a higher temperature cooling stage since at present no single material can cover the cooling from room temperature to 20 K. It is also possible to extract pointers towards improved materials for operation at lower temperatures. The frustrated AFM interactions between the chains in the mineral gaufreyite appear important for its excellent low-field behavior, although PbMnBO_4 appears very good in this respect at its transition temperature of 30 K. The problem with PbMnBO_4 can be traced to two sources: its relatively heavy molecular mass and its high Curie temperature, certainly for operation at 20 K. It seems clear, however, that the strong intra-chain FM interactions both below and above T_c are vital for the properties of the materials studied. We anticipate that the substitution of Pb for a lighter element and weakening slightly the inter-chain magnetic exchange (for a lower T_c) should provide the very best MCE behavior for development as a material for hydrogen liquefaction via energy-efficient adiabatic MC cooling. In addition, we note a molecular field analysis that for quasi-one-dimensional FM chains with weak inter-chain interactions, the 3-dimensional magnetic ordering temperature will vary not only with the inter-chain exchange energy but will also be proportional to the intra-chain correlation length.⁴⁰ Reduction of the intra-chain FM Mn–Mn interactions could be achieved by introducing low concentrations of M^{3+} cations into the chains. These could be either non-magnetic (e.g., Sc^{3+}) or magnetic with configurations that disrupt the 90° FM Mn–O–Mn interactions (e.g., Cr^{3+} or Fe^{3+}). In this way, significantly enhanced MC behavior might be achieved at temperatures close to 20 K.

■ ASSOCIATED CONTENT

Supporting Information

The Supporting Information is available free of charge at <https://pubs.acs.org/doi/10.1021/acs.chemmater.0c03701>.

NPD Rietveld refinement plots for PbMnBO_4 at 300 K; $\text{Pb}_{0.5}\text{Sr}_{0.5}\text{MnBO}_4$ at 300 K; PbMnBO_4 at 35 K in 4 T; PbMnBO_4 at 1.5 K in 2 T; and SrMnBO_4 at 1.5 K in 4.5 T (PDF)

■ AUTHOR INFORMATION

Corresponding Author

Colin Greaves – School of Chemistry, University of Birmingham, Birmingham B15 2TT, United Kingdom; orcid.org/0000-0002-9568-3697; Email: c.greaves@bham.ac.uk

Authors

Jake Head – School of Physics and Astronomy, University of Birmingham, Birmingham B15 2TT, United Kingdom
 Pascal Manuel – ISIS Facility, STFC Rutherford Appleton Laboratory, Didcot OX11 0QX, United Kingdom
 Fabio Orlandi – ISIS Facility, STFC Rutherford Appleton Laboratory, Didcot OX11 0QX, United Kingdom; orcid.org/0000-0001-6333-521X
 Minki Jeong – School of Physics and Astronomy, University of Birmingham, Birmingham B15 2TT, United Kingdom
 Martin R. Lees – Department of Physics, University of Warwick, Coventry CV4 7AL, United Kingdom
 Rukang Li – Beijing Centre for Crystal Research and Development, Key Laboratory of Functional Crystals and Laser Technology, Technical Institute of Physics and

Chemistry, Chinese Academy of Sciences, Beijing 100190, P.R. China; University of Chinese Academy of Science, Beijing 100049, P.R. China; orcid.org/0000-0002-0230-0029

Complete contact information is available at:
<https://pubs.acs.org/10.1021/acs.chemmater.0c03701>

Notes

The authors declare no competing financial interest.

ACKNOWLEDGMENTS

The present work was supported by the National Natural Science Foundation of China (No. 51772304), EPSRC (2285028), and the University of Birmingham (Birmingham Fellowship). The authors acknowledge the Science and Technology Facilities Council (STFC) for the provision of neutron beam facilities. Neutron diffraction data analysed in this report can be obtained at 10.5286/ISIS.E.RB1920247.

REFERENCES

- Qu, Y. H.; Cong, D. Y.; Li, S. H.; Gui, W. Y.; Nie, Z. H.; Zhang, M. H.; Ren, Y.; Wang, Y. D. Simultaneously Achieved Large Reversible Elastocaloric and Magnetocaloric Effects and Their Coupling in a Magnetic Shape Memory Alloy. *Acta Mater.* **2018**, *151*, 41–55.
- Yu, B.; Liu, M.; Egolf, P. W.; Kitanovski, A. A Review of Magnetic Refrigerator and Heat Pump Prototypes Built before the Year 2010. *Int. J. Refrig.* **2010**, *33* (6), 1029–1060.
- Liu, J.; Gottschall, T.; Skokov, K. P.; Moore, J. D.; Gutfleisch, O. Giant Magnetocaloric Effect Driven by Structural Transitions. *Nat. Mater.* **2012**, *11* (7), 620–626.
- Zhang, H.; Shen, B. G.; Xu, Z. Y.; Shen, J.; Hu, F. X.; Sun, J. R.; Long, Y. Large Reversible Magnetocaloric Effects in ErFeSi Compound under Low Magnetic Field Change around Liquid Hydrogen Temperature. *Appl. Phys. Lett.* **2013**, *102* (9), 092401.
- Shinde, K. P.; Jang, S. H.; Ranot, M.; Sinha, B. B.; Kim, J. W.; Chung, K. C. Large Magnetic Entropy Change at Cryogenic Temperature in Rare Earth HoN Nanoparticles. *RSC Adv.* **2016**, *6* (79), 75562–75569.
- Li, R. Enhancing the Magnetocaloric Effect of a Paramagnet to above Liquid Hydrogen Temperature. *Energy Technol.* **2019**, *7* (5), 1801070.
- Numazawa, T.; Kamiya, K.; Utaki, T.; Matsumoto, K. Magnetic Refrigerator for Hydrogen Liquefaction. *Cryogenics* **2014**, *62*, 185–192.
- Campoy, J. C. P.; Plaza, E. J. R.; Coelho, A. A.; Gama, S. Magnetoresistivity as a Probe to the Field-Induced Change of Magnetic Entropy in RAl_2 Compounds ($R=Pr, Nd, Tb, Dy, Ho, Er$). *Phys. Rev. B: Condens. Matter Mater. Phys.* **2006**, *74* (13), 134410.
- Zhitomirsky, M. E. Enhanced Magnetocaloric Effect in Frustrated Magnets. *Phys. Rev. B: Condens. Matter Mater. Phys.* **2003**, *67* (10), 104421.
- Schnack, J.; Schmidt, R.; Richter, J. Enhanced Magnetocaloric Effect in Frustrated Magnetic Molecules with Icosahedral Symmetry. *Phys. Rev. B: Condens. Matter Mater. Phys.* **2007**, *76* (5), 054413.
- Sosin, S. S.; Prozorova, L. A.; Smirnov, A. I.; Golov, A. I.; Berkutov, I. B.; Petrenko, O. A.; Balakrishnan, G.; Zhitomirsky, M. E. Magnetocaloric Effect in Pyrochlore Antiferromagnet $Gd_2Ti_2O_7$. *Phys. Rev. B: Condens. Matter Mater. Phys.* **2005**, *71* (9), 094413.
- Dixey, R. J. C.; Orlandi, F.; Manuel, P.; Mukherjee, P.; Dutton, S. E.; Saines, P. J. Emergent Magnetic Order and Correlated Disorder in Formate Metal-Organic Frameworks. *Philos. Trans. R. Soc., A* **2019**, *377* (2149), 20190007.
- Dixey, R. J. C.; Saines, P. J. Optimization of the Magnetocaloric Effect in Low Applied Magnetic Fields in $LnOHCO_3$ Frameworks. *Inorg. Chem.* **2018**, *57* (20), 12543–12551.
- Dixey, R. J. C.; Stenning, G. B. G.; Manuel, P.; Orlandi, F.; Saines, P. J. Ferromagnetic Ising Chains in Frustrated $LnODCO_3$: The Influence of Magnetic Structure in Magnetocaloric Frameworks. *J. Mater. Chem. C* **2019**, *7* (42), 13111–13119.
- Saines, P. J.; Paddison, J. A. M.; Thygesen, P. M. M.; Tucker, M. G. Searching beyond Gd for Magnetocaloric Frameworks: Magnetic Properties and Interactions of the $Ln(HCO_2)_3$ Series. *Mater. Horiz.* **2015**, *2* (5), 528–535.
- Hoffmann, C.; Armbruster, T.; Kunz, M. Structure Refinement of (001)Disordered Gaufreyite $Ca_4Mn^{3+}_3[(BO_3)_3(CO_3)_3]_3$: Jahn-Teller-Distortion in Edge-Sharing Chains of $M^{3+}O_6$ Octahedra. *Eur. J. Mineral.* **1997**, *9* (1), 7–20.
- Li, R.; Li, G.; Greaves, C. Gaufreyite: A Mineral with Excellent Magnetocaloric Effect Suitable for Liquefying Hydrogen. *J. Mater. Chem. A* **2018**, *6* (13), 5260–5264.
- Li, R.; Manuel, P.; Orlandi, F.; Greaves, C. Magnetic Ordering of the Cryogenic Magnetic Cooling Mineral Gaufreyite. *J. Mater. Chem. A* **2018**, *6* (42), 21149–21155.
- Park, H.; Lam, R.; Greedan, J. E.; Barbier, J. Synthesis, Crystal Structure, Crystal Chemistry, and Magnetic Properties of $PbMBO_4$ ($M = Cr, Mn, Fe$): A New Structure Type Exhibiting One-Dimensional Magnetism. *Chem. Mater.* **2003**, *15* (8), 1703–1712.
- Koo, H.-J.; Whangbo, M.-H. Density Functional Investigation of the Magnetic Properties of $PbMBO_4$ ($M=Cr, Mn, Fe$). *Solid State Commun.* **2009**, *149* (15-16), 602–604.
- Xiang, H.; Tang, Y.; Zhang, S.; He, Z. Intra-Chain Superexchange Couplings in Quasi-1D 3d Transition-Metal Magnetic Compounds. *J. Phys.: Condens. Matter* **2016**, *28* (27), 276003.
- Pankrats, A.; Kolkov, M.; Martynov, S.; Popkov, S.; Krasikov, A.; Balaev, A.; Gorev, M. Peculiarities of a Magnetic Transition in a Quasi-One-Dimensional Ferromagnet $PbMnBO_4$. *J. Magn. Magn. Mater.* **2019**, *471*, 416–422.
- Pankrats, A.; Sablina, K.; Eremin, M.; Balaev, A.; Kolkov, M.; Tugarinov, V.; Bovina, A. Ferromagnetism and Strong Magnetic Anisotropy of the $PbMnBO_4$ Orthoborate Single Crystals. *J. Magn. Magn. Mater.* **2016**, *414*, 82–89.
- Chapon, L. C.; Manuel, P.; Radaelli, P. G.; Benson, C.; Perrott, L.; Ansell, S.; Rhodes, N. J.; Raspino, D.; Duxbury, D.; Spill, E.; Norris, J. Wish: The New Powder and Single Crystal Magnetic Diffractometer on the Second Target Station. *Neutron News* **2011**, *22* (2), 22–25.
- Toby, B. H.; Von Dreele, R. B. GSAS-II: The Genesis of a Modern Open-Source All Purpose Crystallography Software Package. *J. Appl. Crystallogr.* **2013**, *46* (2), 544–549.
- Pecharsky, V. K.; Gschneidner, K. A. Magnetocaloric Effect from Indirect Measurements: Magnetization and Heat Capacity. *J. Appl. Phys.* **1999**, *86* (1), 565–575.
- Shannon, R. D. Revised Effective Ionic Radii in Halides and Chalcogenides. *Acta Crystallogr., Sect. A: Cryst. Phys., Diff., Theor. Gen. Crystallogr.* **1976**, *A32*, 751–767.
- Brown, I. D.; Altermatt, D. Bond-Valence Parameters Obtained from a Systematic Analysis of the Inorganic Crystal Structure Database. *Acta Crystallogr., Sect. B: Struct. Sci.* **1985**, *41* (4), 244–247.
- Mentré, O.; Dhaussy, A. C.; Abraham, F.; Suard, E.; Steinfink, H. Crystal Structure of $Pb_2V_3O_9$: Rietveld Refinement and Electron Lone-Pair Localization. The Magnetic Susceptibility of Sr^{2+} -Substituted Phases. *Chem. Mater.* **1999**, *11* (9), 2408–2416.
- Miller, S.; Love, W. F. *Tables of Irreducible Representations of Space Groups and Co-Representations of Magnetic Space Groups*; Pruett: Boulder, CO, 1967.
- Taroni, A.; Bramwell, S. T.; Holdsworth, P. C. W. Universal Window for Two-Dimensional Critical Exponents. *J. Phys.: Condens. Matter* **2008**, *20* (27), 275233.
- Bramwell, S. T.; Holdsworth, P. C. W. Universality in Two-dimensional Magnetic Systems. *J. Appl. Phys.* **1993**, *73* (10), 6096–6098.
- Ghatak, S. K.; Chaudhuri, I. A Possible Mechanism for Large Magnetostriction in Manganite System. *J. Magn. Magn. Mater.* **2003**, *261* (3), 442–448.

(34) Dionne, G. F. Origin of the Magnetostriction Effects from Mn^{3+} , Co^{2+} , and Fe^{2+} Ions in Ferrimagnetic Spinels and Garnets. *J. Appl. Phys.* **1979**, *50* (6), 4263–4272.

(35) Goodenough, J. B. Theory of the Role of Covalence in the Perovskite-Type Manganites $[La,M(II)]MnO_3$. *Phys. Rev.* **1955**, *100* (2), 564–573.

(36) Kanamori, J. Superexchange Interaction and Symmetry Properties of Electron Orbitals. *J. Phys. Chem. Solids* **1959**, *10* (2-3), 87–98.

(37) Anderson, P. W. New Approach to the Theory of Superexchange Interactions. *Phys. Rev.* **1959**, *115* (1), 2–13.

(38) Whangbo, M. H.; Koo, H. J.; Dai, D.; Jung, D. Interpretation of the Magnetic Structures of $Cu_2Te_2O_5X_2$ ($X = Cl, Br$) and $Ca_{3.1}Cu_{0.9}RuO_6$ on the Basis of Electronic Structure Considerations: Cases for Strong Super-Superexchange Interactions Involving Cu^{2+} Ions. *Inorg. Chem.* **2003**, *42* (12), 3898–3906.

(39) Koo, H. J.; Dai, D.; Whangbo, M. H. Importance of Supersuperexchange Interactions in Determining the Dimensionality of Magnetic Properties. Determination of Strongly Interacting Spin Exchange Paths in a $A_2Cu(PO_4)_2$ ($A = Ba, Sr$), $ACuP_2O_7$ ($A = Ba, Ca, Sr, Pb$), $CaCuGe_2O_6$ and $Cu_2UO_2(PO_4)_2$ on the basis of Qualitative Spin Dimer Analysis. *Inorg. Chem.* **2005**, *44* (12), 4359–4365.

(40) de Jongh, L. J. Introduction to Low-Dimensional Magnetic Systems. In *Magnetic Properties of Layered Transition Metal Compounds*; de Jongh, L. J., Ed.; Kluwer Academic Publishers: Dordrecht, 1990; pp 1–51.